Surrogate based shape optimization and uncertainty assessment of a ERCOFTAC pump

Alessia Fracassi, Remo de Donno, Antonio Ghidoni, Pietro Marco Congedo

ARTICLE TEMPLATE

Surrogate based shape optimization and uncertainty assessment of a ERCOFTAC pump

A. Fracassi[a], R. De Donno[b], A. Ghidoni[a] and P. M. Congedo[c]

[a]Department of Mechanical and Industrial Engineering (DIMI), University of Brescia, via Branze 38, 25123 Brescia; [b]Industrie Saleri Italo S.p.A., via Ruca 406, 25065 Lumezzane (BS), Italy; [c]DEFI Team (INRIA Saclay Île-de-France and Ecole Polytechnique), CMAP, 1 rue d'Estienne d'Orves, 91120 Palaiseau, France

ARTICLE HISTORY
Compiled April 8, 2020

ABSTRACT
Centrifugal pumps, being used nowadays for many applications, must be suited for a wide range of pressure ratios and flow rates. To overcome difficulties arising from the design and performance prediction of this class of turbomachinery, many researchers proposed the coupling of CFD codes and optimization algorithms for a fast and effective design procedure. However, uncertainties are present in most engineering applications such as turbomachines, and their influence on turbomachinery performance should be considered. In this work we apply some advanced optimization techniques to the blade optimization of an ERCOFTAC-like pump, and we assess the robustness of the optimal profiles through an uncertainty propagation study. The main source of uncertainty is constituted by the uncertainty of the operating conditions, primarily the rotational speed of the pump shaft that affects also the flow rate.

KEYWORDS
centrifugal pump, uncertainty, shape optimization, surrogate model, genetic algorithm, ERCOFTAC pump

1. Introduction

Centrifugal pumps, being used nowadays for many applications, must be suited for a wide range of pressure ratios and flow rates. Their design and performance prediction is not an easy task, being influenced by many free geometric parameters. Experimental approaches based on the modification of prototypes and/or previous models and numerical approaches based on CAD/CFD tools have been applied to their design and analysis. However, the former approach is expensive and time-consuming, while the latter make available many data which are not easily related to the pump performance, making difficult the improvement of the pump.

In the last decade, to overcome the problems shown by the previous techniques, many researchers proposed the coupling of CFD codes and optimization algorithms for the design of turbomachinery [1, 2, 3, 4, 5]. This approach has been also successfully applied to the pump design [6, 7, 8].

CONTACT A. Fracassi. Email: a.fracass004@unibs.it

Table 1.: Main dimensions of the ERCOFTAC pump

Impeller	
inlet blade diameter	$D_1 = 240$ mm
outlet blade diameter	$D_2 = 420$ mm
number of blades	$z_i = 7$
Diffuser	
inlet vane diameter	$D_3 = 444$ mm
outlet vane diameter	$D_4 = 664$ mm
number of vanes	$z_d = 12$

Table 2.: Approximation error [%] for different reference camber-lines and order of the Bezier curves

	3^{rd}	4^{th}	5^{th}
Impeller ERC	0.518	0.156	0.065
Vaned diffuser ERC	0.210	0.0558	0.0457
NACA 63	0.853	0.266	0.105
NACA 64	0.440	0.0946	0.0640
NACA 65	0.127	0.0131	0.000993
DCA	0.182	0.0474	0.0104
C4	0.0115	0.00108	1.71E-05

However, uncertainties are present in most engineering applications such as turbomachines. The performance of turbomachinery can be highly affected by the presence of uncertainties and these effects should be considered in a robust design procedure [9], *i.e.*, less sensitive to the system uncertainties. In particular in this work an optimal blade profile for the ERCOFTAC pump is obtained with a deterministic optimization and the robustness of this optimal profile is assessed through an uncertainty propagation study. The main source of uncertainty is constituted by the rotational speed of the pump shaft and the losses in the cooling system, both affecting also the flow rate.

In the following, Sec. 2 is devoted to the description of the geometric parametrization algorithm, Sec. 3 describes the CFD solver, while Sec. 4 and 6 describe the optimization algorithm and the framework for the uncertainty quantification assessment, respectively. Section 5 and 7 present the results.

2. Geometric parameterization

The parameterization algorithm allows to represent the blade geometry of the impeller and vaned diffuser as a combination of the camber-line and thickness distribution. 18 design variables are used to parameterize the complete geometry. The inlet and outlet diameters of the impeller blades are fixed, together with the inlet diameter of the vaned diffuser. The diameter of the diffuser trailing edge is instead free to shorten, remaining fixed the discharge location. The algorithm can reproduce the ERCOFTAC blades, but with smooth profiles. The main dimensions of the ERCOFATC pump are summarized in Tab. 1.

2.1. *Camber-line*

The camber-lines of the impeller and the diffuser are described through a Bézier curve. To define the most suitable number of control points, i.e. the order of the Bézier curve, 3^{rd}, 4^{th} and 5^{th} order curves are considered. The purpose is to use the minimum number of input variables to represent the camber-line of the ERCOFTAC pump blades and of profile commonly used to manufacture pump blades, *i.e.* the NACA 6-series, the double circular arc (DCA) and the C4 airfoil. These curves are built leaving two degrees of freedom for each control point inside the curve. The approximation error has been measured by evaluating the distance (root mean square distance normalized with the chord length) between the real and parametrized profiles, and is reported in Tab. 2

Table 3.: List of the design variables, description, baseline value, minimum and maximum value during the optimization

Variable	Description	Baseline	Min value	Max value
γ_{imp}	Stagger angle of the impeller [°]	-111.5	120	-90
β_1	Inlet angle of the impeller [°]	-66.0	-76	-56
β_2	Outlet angle of the impeller [°]	-70.9	-75	-60
γ_{dif}	Stagger angle of the diffuser [°]	101.4	90	105
α_3	Inlet angle of the diffuser [°]	72.8	65	85
α_4	Outlet angle of the diffuser [°]	67.8	60	75
x_{t_LEi}	Position along the chord of point of maximum thickness at leading edge of impeller [-]	0.1330	0.1	0.3
$dr_{LE,i}$	Difference between x_{t_LEi} and the radius at leading edge of the impeller [-]	0.06323	0.010	0.064
$k_{t,i}$	Curvature at the point of maximum thickness at leading edge of the impeller [-]	-3.2591	-3.26	-1.00
$x_{t\_TE,i}$	Position along the chord of the point of maximum thickness at trailing edge of the impeller [-]	0.9146	0.80	0.95
$x_{3\_TE,i}$	Position along the chord of the third control point at trailing edge of the impeller [-]	0.9323	0.92	1.00
$\alpha_{TE,i}$	Slope at trailing edge of the impeller	-0.9556	-1.2	-0.5
$x_{t\_LE,d}$	Position along the chord of the point of maximum thickness at leading edge of the diffuser [-]	0.1424	0.1	0.3
$dr_{LE,d}$	Difference between x_{t_LEd} and the radius at leading edge of the diffuser [-]	0.01008	0.005	0.100
$y_{1\_LE,d}$	Thickness at leading edge of the diffuser [-]	4.0129	2.0	5.0
$\alpha_{LE,d}$	Slope at leading edge of the diffuser [-]	0.004266	0.003	0.075
$x_{t\_TE,d}$	Position along the chord of the point of maximum thickness at trailing edge of the diffuser [-]	0.999	0.700	0.999
D_4	Outlet diameter of the diffuser blade [mm]	664.0	554.0	664.0

for each reference camber-line considered.

A fourth order Bézier curve has been chosen for the parameterization, characterized by a number of degrees of freedom equal to a third order curve. In fact, during the optimization the distance of the two internal control points from the leading and trailing edge is fixed and equal to the corresponding distance for the ERCOFTAC geometry, while inlet and outlet angles of the blades can change. This choice allows for a better approximation of the ERCOFTAC camber-lines and for a higher geometrical flexibility than a standard third order curve, even if sharing the same number of variables. The approximation error is comparable to a third order curve.

In addition to inlet and outlet angles during the optimization also the stagger angles are variable.

2.2. *Thickness function*

The thickness function is parametrized in different way for the impeller and the diffuser to better fit the thickness function of the ERCOFTAC blades. In both cases the leading and the trailing edge are described through a Bézier curve and they are joined with a constant thickness line (see Fig. 1).

The control points are set according to the following formulas:

- **Impeller leading edge**

$$s_{1\_LE} = 0 \qquad t_{1\_LE} = 0$$
$$s_{2\_LE} = 0 \qquad t_{2\_LE} = 3k_{t,i}\frac{dr_{LE,i}^2}{2} + \hat{y}_{t,i}$$
$$s_{3\_LE} = x_{t\_LE,i} - dr_{LE,i} \qquad t_{3\_LE} = \hat{y}_{t,i}$$
$$s_{4\_LE} = x_{t\_LE,i} \qquad t_{4\_LE} = \hat{y}_{t,i}$$

- **Impeller trailing edge**

$$s_{1\_TE} = c_i \qquad t_{1\_TE} = \hat{y}_{TE,i}$$
$$s_{2\_TE} = c_i + \frac{\hat{y}_{2\_TE,i} - \hat{y}_{TE,i}}{\tan(\alpha_{TE,i})} \qquad t_{2\_TE} = \hat{y}_{2\_TE,i}$$
$$s_{3\_TE} = x_{3\_TE,i} \qquad t_{3\_TE} = \hat{y}_{3\_TE,i}$$
$$s_{4\_TE} = x_{t\_TE,i} + dr_{LE,i} \qquad t_{4\_TE} = \hat{y}_{t,i}$$
$$s_{5\_TE} = x_{t\_TE,i} \qquad t_{5\_TE} = \hat{y}_{t,i}$$

- **Vaned diffuser leading edge**

$$s_{1\_LE} = 0 \qquad t_{1\_LE} = y_{1\_LE,d}$$
$$s_{2\_LE} = x_{2\_\hat{L}E,d} \qquad t_{2\_LE} = \frac{\hat{x}_{2\_LE,d}}{\tan(\alpha_{LE,d})} + y_{1\_LE,d}$$
$$s_{3\_LE} = x_{t\_LE,d} - dr_{LE,d} \qquad t_{3\_LE} = \hat{y}_{t,d}$$
$$s_{4\_LE} = x_{t\_LE,d} \qquad t_{4\_LE} = \hat{y}_{t,d}$$

- **Vaned diffuser trailing edge**

$$s_{1\_TE} = c_d \qquad t_{1\_TE} = \hat{y}_{1\_TE,d}$$
$$s_{2\_TE} = c_d \qquad t_{2\_TE} = \hat{y}_{t,d}$$
$$s_{3\_TE} = x_{t\_TE,d} \qquad t_{3\_TE} = \hat{y}_{t,d}$$

The definition of the input variables is reported in Tab. 3, where the letter c is the chord length, the subscripts i and d refer to the impeller and the diffuser, respectively. The hat symbol defines a fixed value. In particular, $\hat{y}_t$ is the maximum thickness of the blade, which is set equal to the thickness of ERCOFTAC blade to compare different profiles and to avoid the computation of too thin blades.

2.3. *Range of the input variables*

The ERCOFTAC geometry is considered as the baseline configuration for the optimization process, and the corresponding values of the input variables are found optimizing the position of the control points to minimize the approximation error (root mean square distance between corresponding points of the real and parametrized geometry).

The range of the input variables for the optimization (see Tab. 3) is built ensuring three constraints: i) input values defining the baseline geometry are included, ii) not feasible geometries cannot be generated in the Design of Experiment (DoE), and iii) blade angles which are supposed to be close to the optimum, are included. In particular, the impeller inlet angle is calculated through velocity diagrams, while a common range for impeller outlet angles has been taken from literature. The range of diffuser inlet angles is computed from the impeller outlet angles, applying velocity diagrams, while the range for diffuser outlet angles is computed starting from the volute outlet velocity,

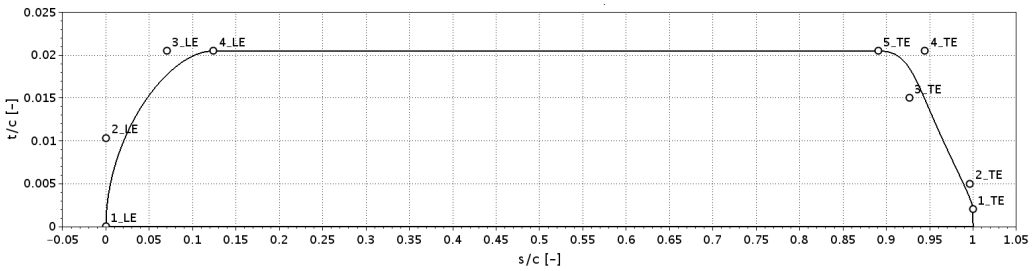

(a) *Impeller*

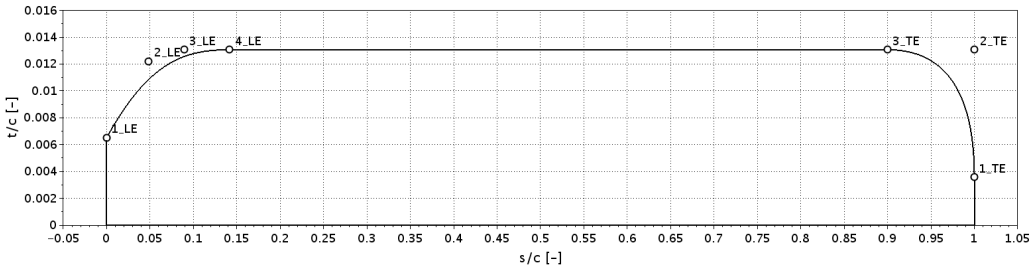

(b) *Vaned diffuser*

Figure 1.: Control points for the thickness function parameterization

estimated with the Stepanoff theory [10], and assuming the flow in the volute satisfies the free-vortex theory.

The comparison between real and parametrized ERCOFTAC geometry is shown in Figs. 2 and 3.

3. CFD

The 2D hybrid meshes of the geometries created during the optimization process are generated with an in-house mesh generator [11]. Only one blade passage is considered for the impeller and diffuser. The size of the elements adjacent to the solid walls is equal to a non-dimensional distance $y^+ \approx 1$, to compute the boundary layer accurately up to the wall.

The open-source CFD toolbox OpenFOAM [12] is used to compute the flow field in the pump. The incompressible Reynolds Averaged Navier-Stokes (RANS) equations coupled with k-ω SST turbulence model [13] are solved. The choice of the turbulence model is dictated by the SST capability to predict correctly flow-fields characterized by adverse pressure gradient and/or detachment, *i.e.* the expected flow-field of a pump.

On the basis of previous studies [14, 15], which demonstrate the capability of 2D simulations to predict fairly well the ERCOFTAC pump flow-field, 2D simulations have been chosen also for this work to reduce the computational effort.

The operating conditions are summarized in Tab. 4. At the domain inlet the velocity V_1 (computed from ϕ), the turbulence intensity $Tu_1 = 4\%$ and specific dissipation rate ω_1 are prescribed, while at the outflow a static pressure is set. Adiabatic wall boundary conditions are applied to all blades.

A steady-state formulation with the Multiple Reference Frame (MRF) approach is used; the impeller and diffuser are fixed with respect to each other, but the momentum equation for the impeller domain is computed in the rotating reference frame. A mixing-plane interface is applied between the impeller and the diffuser. This approach

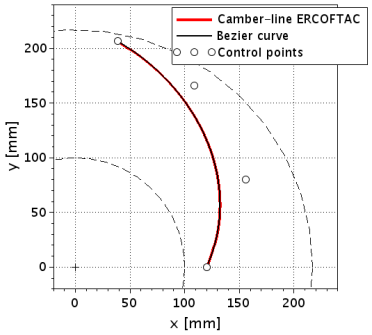

(a) *Impeller*

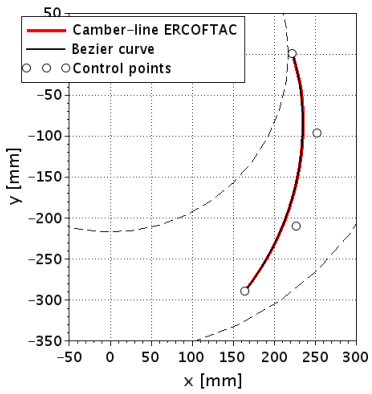

(b) *Vaned diffuser*

Figure 2.: Control points of the parameterized ERCOFTAC camber-lines

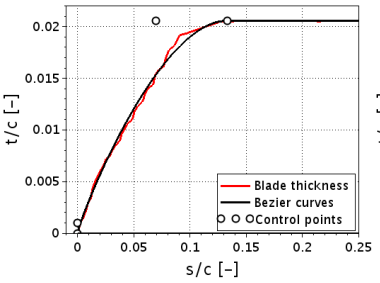

(a) *Impeller leading edge*

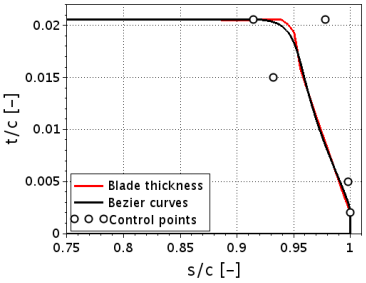

(b) *Impeller trailing edge*

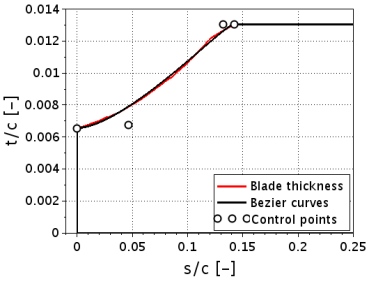

(c) *Vaned diffuser leading edge*

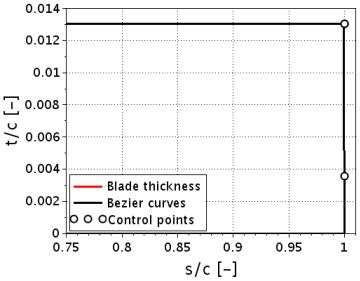

(d) *Vaned diffuser trailing edge*

Figure 3.: Control points of the parameterized ERCOFTAC thickness function

avoid the convection of non-physical wakes created by the impeller blades through the pump, typical problem of the frozen rotor interface. The use of the mixing plane interface allows the simulation of a single blade passage for both impeller and vaned diffuser, reducing significantly the computational cost. Mixing plane and frozen rotor interfaces have been compared in terms of predicted ψ and η with an unsteady simulation for the 3D ERCOFTAC pump. Table 5 summarizes the results, showing a good agreement between the mixing-plane and unsteady simulations, both in terms of efficiency and total pressure coefficient.

The second-order upwind discretization scheme is applied to the divergence of the velocity, while the first-order upwind scheme is applied to the turbulent quantities. The Laplacian terms are evaluated using a linear second-order bounded central scheme,

Table 4.: Operating conditions of the ERCOFTAC pump

Operating conditions	
rotational speed	$n = 2000rpm$
flow rate coefficient	$\phi = \frac{4Q}{\pi D_2^2 U_2} = 0.048$
Reynolds number	$Re = 6.5\ 10^5$
Inlet air reference conditions	
temperature	$T = 298K$
air density	$\rho = 1.2\ kg/m^3$

Table 5.: Comparison of different approaches to simulate impeller/diffuser interface for the prediction of η and ψ of the 3D ERCOFTAC pump

CFD approach	ψ [-]	η [%]
unsteady	0.748	87.3
steady-state + Forzen rotor	0.730	84.4
steady-state + Mixing plane	0.764	87.0

Table 6.: Predicted η and ψ for the real and parametrized ERCOFTAC pump geometry, mesh with about 37000 elements

Geometry	ψ [-]	η [%]
real	0.833	90.0
parametrized	0.891	91.5

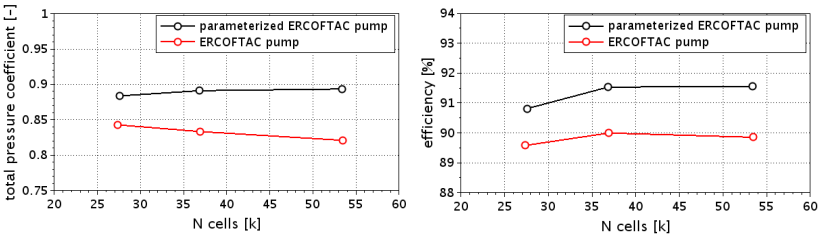

Figure 4.: Grid convergence study for the real and parametrized ERCOFTAC pump geometry

while a central differencing method approximates the gradient term.

3.1. *Performance of the real and parametrized ERCOFTAC pump*

The effect of the geometric parametrization in the prediction of the ERCOFTAC pump performance is first investigated, comparing the predicted η and ψ with the real and parametrized geometry. A mesh convergence study has been proposed for both geometries, using four grids with the number of elements ranging from 25000 to 55000. Finer meshes have been obtained refining uniformly the coarser mesh. The grid convergence study (see Fig. 4) shows some differences in the predicted results, which can be ascribed to the smooth representation of some geometric details given by the parametrization algorithm. As suggested by the convergence study, the grid with 37000 elements ensures a good compromise between computing time and accuracy of the results, and, therefore, it is chosen for the optimization. For this grid, the difference in the predicted η and ψ for the real and parametrized geometry is summarized in Tab. 6.

An in-depth comparison between the two geometries can be obtained looking at the computed flow-fields. In particular Figure 5 and 6 show the pressure contours and the velocity streamlines. The main differences are gathered near the leading and trailing edge, where the parameterization smooths the edges of the original geometry and improve the performances of the pump.

To reproduce the exact original geometry, the presence of straight edges in the profile should be enforced. This would lead to a reduction in the performance of the final optimized geometry. However, being the objective of this work the maximization of the pump performance, the parameterization has been not changed and the parametrized geometry is chosen as baseline to be optimized, instead of the original one.

4. Optimization strategy

In a centrifugal pump, the hydraulic efficiency η and the total pressure rise coefficient ψ have a fundamental role, and, therefore, are chosen as optimization objective and constraint, respectively. In particular the optimization algorithm maximizes η, while keeping ψ constrained to the considered operating conditions. The efficiency η is defined as the ratio between useful hydraulic power and the provided power, while the total pressure rise coefficient is defined as $\psi = \frac{2(p_{out}-p_{in})}{\rho U_2}$, where the subscript *out* refers to the pump outlet, *in* to the pump inlet, and 2 to the impeller outlet. Usually, the pressure head is constrained with a tolerance about $\pm 5\%$, to keep fixed the working

(a) *Pressure contours* **(b)** *Velocity streamlines*

Figure 5.: Pressure and velocity fields of the real ERCOFTAC pump geometry

(a) *Pressure contours* **(b)** *Velocity streamlines*

Figure 6.: Pressure and velocity fields of the parametrized ERCOFTAC pump geometry

condition for the baseline and optimized geometry. However, a numerical investigation has shown that the maximum efficiency is always reached for the upper limit of the constraint, meaning that under uncertainty the constraint could not be guaranteed. Therefore, in the present work only a -5% constraint has been considered for ψ.

Global optimization algorithms require a high number of evaluations in the search of optimum, specially with a high number of input variables. To reduce the computational cost a Surrogate Based Optimization (SBO) [16] is employed. It exploits a surrogate model, that approximates and replaces the underlying truth model for the optimization. Indeed, the evaluations required by the algorithm are analytically computed using the surrogate model, which requires a negligible computational time with respect to a CFD simulation (truth model). A data fit type surrogate (applied here) is an approximation based on the interpolation or regression of a data set from the original model. An initial design of experiments (DoE), is generated through the Latin Hypercube Sampling (LHS) method and each design is analyzed exploiting a CFD simulation. Then a surrogate model is generated from the DoE.

The objective is to compare two different strategies to compute a SBO. The first strategy involves the optimization with a Single Objective Genetic Algorithm (SOGA) applied on the surrogates, while the second one is the Efficient Global Optimization (EGO) [19]. Anyway the algorithms available in the software Dakota [20] are used.

For the first strategy different types of surrogate, available in literature, could be used. Here the Gaussian process or Kriging (KRG) model [17] is applied because it is suitable for both linear and non-linear objective function, it reduces the number of model parameters if the data-set is small [18], and it is often adopted for turbomachin-

ery optimization. This model performs global approximation involving interpolation as following:

$$\hat{f}(\underline{x}) = \underline{g}(\underline{x})^T \underline{\beta} + \epsilon(\underline{x})$$

The objective function $\hat{f}(\underline{x})$ is computed as the sum of trend basis functions (here polynomials) that fits the DoE and a stochastic function $\epsilon(x)$ with mean zero that fix the function to interpolate the experiments. $\underline{g}(\underline{x})$ is the vector of the basis functions, $\underline{\beta}$ is the vector of the generalized least squares estimates of the basis function coefficients and $\epsilon(x)$ is computed using a Gaussian correlation function.

A global optimization algorithm is applied on the surrogate. A Genetic algorithm is chosen cause its flexibility and robustness. It has a low probability to remain trapped in a local minimum and it is often used in turbomachinery shape optimization. Genetic algorithms are based on the mechanism of natural selection and Darwins survival of the fittest concept. A starting population of a fixed number of individuals, evolves by selection, crossover and mutation until a final individual. Each individual is characterized by a vector of settled input variable, that represents a chromosome. Selection is based on individuals fitness, evaluated on the basis of the related objective function value. The individual with the best fitness are chosen as starting point for the following operations. The main mechanism that allows to evolve from a population to an other one is the crossover. It obtains new individuals exchanging portions of chromosomes of two parents. After the crossover the mutation alters randomly part of the chromosomes of some individuals. This avoids the algorithm remain trapped in a local optimum. The percentage of the population which these mechanisms are applied to are respectively 80% and 10%. If the best individual of the starting population is lost by these mechanisms it replaces randomly an individual of the new generation. The process continues until convergence.

The KRG model gives information about the prediction of the objective function and also about the error of this prediction through a Gaussian distribution. The purpose of EGO is to exploit this feature. It is based on a particular version of the Gaussian process model, called DACE [], and it searches the optimum optimizing the Expected Improvement Function (EIF), defined as follows.

$$E[I(\underline{x})] = (f_{max} - \hat{y})\Phi(\frac{f_{max} - \hat{y}}{s}) + s\omega(\frac{f_{max} - \hat{y}}{s})$$

$\hat{y}$ is the predicted function and s is its standard error, while $\Phi(\cdot)$ and $\omega(\cdot)$ are the standard normal density and distribution function.

The performances of the optimum found with one of the previous strategies, are verified with a CFD simulation and the design is added to the DoE. Then the surrogates are updated, iterating until convergence.

The EGO algorithm allows to combine exploitation and exploration, so that both zones with good solutions and zones with lack of information are tested. This could bring advantages to find the global optimum, respect to SBO with SOGA. This latter approach, in facts, focuses the research only in the zone of good prediction, but to not consider the error of the surrogate far away this area can leads to obtain local optimum, in particular when the huge number of design variables could lead to accuracy problems in the definition of the response surface. On the other hand the EGO algorithm requires to find the optimum of a more complex function.

5. Deterministic optimization results

The initial DoE is constituted by 340 designs, distributed over the whole domain with the LHS. Each design is analyzed exploiting a CFD simulation and it is excluded if the CFD calculation does not converge or the solution may not be reliable. Subsequently 298 design are considered for the DoE, being feasible. SBO with a SOGA algorithm and EGO have been applied to this DoE to optimize the pump efficiency.

During the optimization process, the convergence can be affected by the presence of not reliable design. This issue is addressed differently for the two strategies. In the SOGA optimization a dummy output is returned, characterized by $\eta = 70\%$ and $\psi = 0.7$. The efficiency value must be lower than the optimum; this value must be chosen carefully because too small values can deteriorate the accuracy of the surrogate model. The value of the pressure coefficient is selected just outside the constraint. After a set of iterations, the designs that are not reliable are removed, and the process is reinitialized. For the EGO approach a dummy output can not be used, always creating instability issues. Therefore, if an unreliable design is found, a reliable one is evaluated in the neighborhood and replaced.

In Fig. 7 the convergence history for the SOGA and the EGO strategy are shown. Here the maximum efficiency found by the algorithms at each iteration is plotted. After about 200 iterations the optimizations are stopped, because in both cases the convergence is supposed to be reached. Hence, the SOGA optimization reaches the convergence in about 130 iterations and five reinitializations, with a maximum efficiency $\eta_{S,max} = 94.4\%$ and a $\psi_S = 0.891$. The EGO converges in about the same number of iterations, reaching the maximum efficiency $\eta_{E,max} = 94.6\%$ with $\psi_E = 0.890$. In Fig. 8 the evaluated design for the two strategies on the chart $\psi - \eta$ are shown, while in Fig. 9 the same evaluations are represented in the input space. It can be noted as the EGO algorithm scouts a larger space than the SOGA.

In Fig. 10 a comparison between the baseline and optimized geometries is shown. In particular the SOGA optimum presents a more tapered impeller blade, a lower chord length of the diffuser and a more rounded trailing edge for the diffuser. These features reduce losses, especially at the trailing edge of the impeller, where the speed is lowered, and at the leading edge of the diffuser, where the flow detachment of the baseline geometry is not present (see Fig. **??**). In Tab. 7 the design variables of the two optimum are compared.

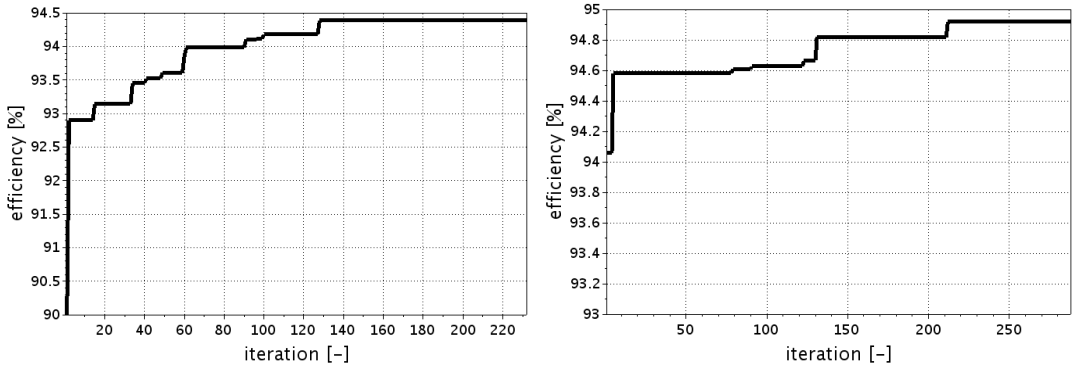

Figure 7.: Convergence history for SBO with SOGA algorithm (left) and EGO (right)

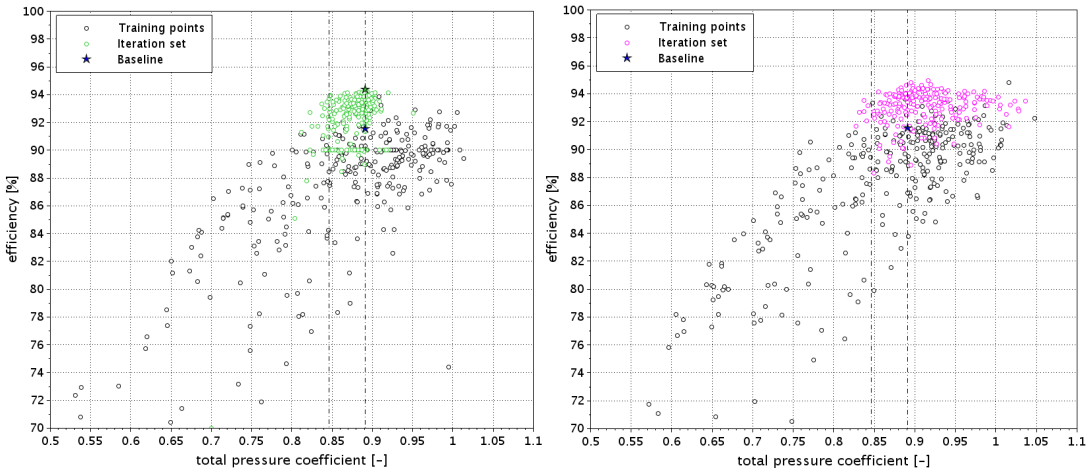

(a) *SBO with SOGA* **(b)** *EGO*

Figure 8.: Design evaluations in the optimization processes

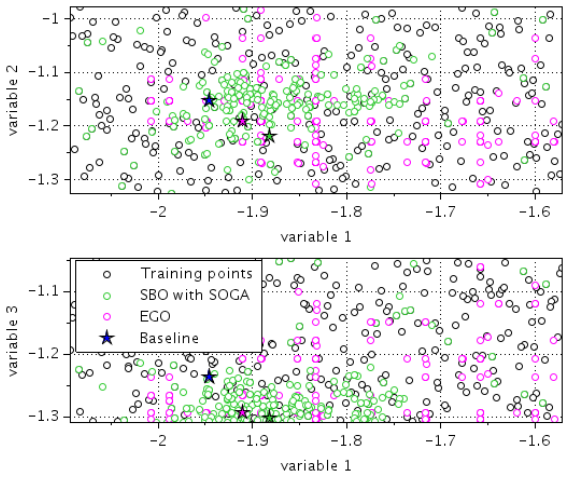

Figure 9.: Position of the evaluations during the optimization processes. Variable 1 is the stagger angle, Variable 2 is the inlet angle, Variables 3 is the outlet angle, of the impeller blades. The stars show the position of the baseline and the optimum for the two strategies.

Table 7.: Values of the design variables for the two optima

Variable	SBO with SOGA optimum	EGO optimum
γ_{imp}	-107.8	-109.4
β_1	-69.9	-68.2
β_2	-74.7	-74.2
γ_{dif}	94.3	97.5
α_3	75.1	70.6
α_4	64.5	64.2
x_{t_LEi}	0.2589	0.1556
$dr_{LE,i}$	0.02725	0.06100
$k_{t,i}$	-3.0502	-3.1344
$x_{t\_TE,i}$	0.8140	0.8417
$x_{3\_TE,i}$	0.9362	0.9244
$\alpha_{TE,i}$	-0.6415	-0.7722
$x_{t\_LE,d}$	0.2156	0.1778
$dr_{LE,d}$	0.01899	0.03139
$y_{1\_LE,d}$	2.0050	2.0556
$\alpha_{LE,d}$	0.07476	0.007000
$x_{t\_TE,d}$	0.7809	0.9244
D_4	593.9	

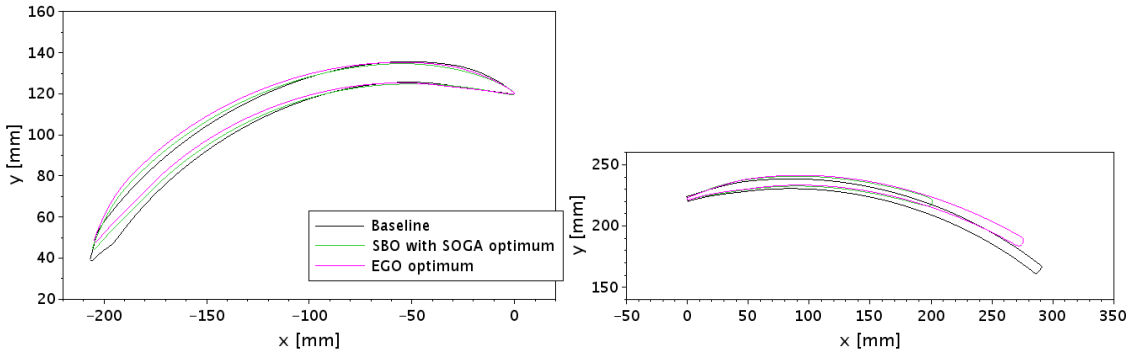

(a) *Impeller* **(b)** *Vaned diffuser*

Figure 10.: Comparison between the baseline and the optimized geometry

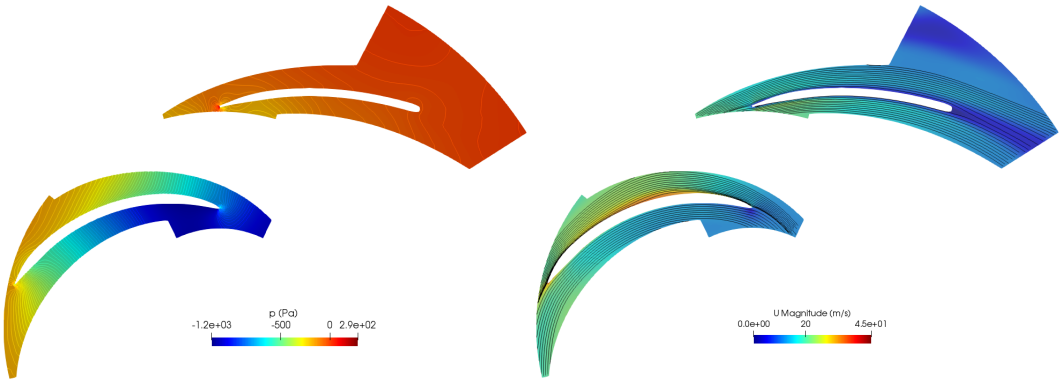

(a) *Pressure contours* **(b)** *Velocity streamlines*

Figure 11.: Pressure and velocity fields of the SOGA optimized geometry

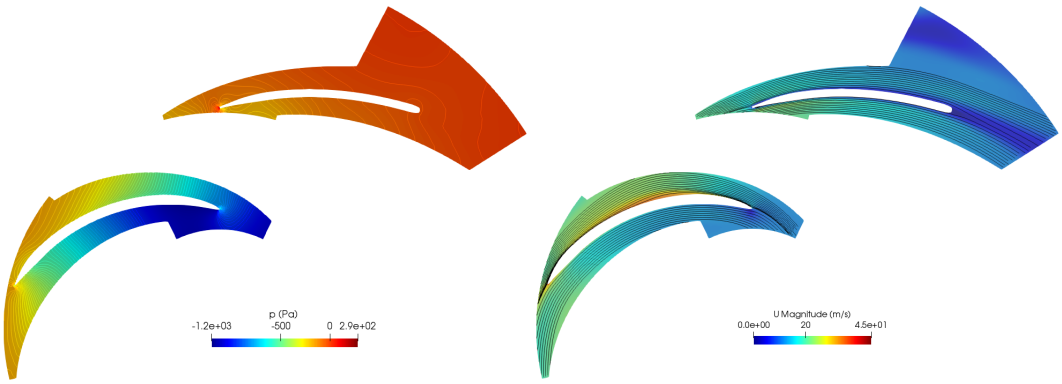

(a) *Pressure contours* **(b)** *Velocity streamlines*

Figure 12.: Pressure and velocity fields of the EGO optimized geometry

Table 8.: Uncertain variables

Uncertain variable	Deterministic value	Uncertainty range
Rotational speed N	$2000rpm$	$\pm 5rpm$
System resistance a	$1.21 \cdot 10^5 Pa \cdot s/m^3$	$\pm 5\%$
Turbulent intensity I	5%	$0.1 - 10\%$
Viscosity ratio $\frac{\mu_T}{\mu}$	10	$0.1 - 50$

6. Uncertainty Quantification assessment

Even if an optimal design is reached in a deterministic environment, the real performance of the optimized pump could be different, due to the presence of uncertainties, which can be found in most engineering applications.

The purpose of this work is to assess the robustness of the deterministic optimum for a centrifugal pump under uncertain boundary conditions. In facts, after a preliminary design, the pump is manufactured and tested in a test rig to verify the total pressure head and the efficiency, but the boundary condition applied to the pump are subject to uncertainty. To ensure the significance of the optimization study presented above it's worthwhile to estimate how the uncertainties that affect the pump test impact the performances and how this impact changes modifying the design. The uncertainties here considered are of two type: on the one hand there are boundary condition that can be managed with the test rig set-up and on the other one CFD conditions that cannot be experimentally controlled and are not even available as measurement.

The pump rotates at the operating rotational speed, and is plugged in a hydraulic system, whose resistance is chosen to provide the operating mass flow rate. Uncertainties of the first type are the rotational speed and the hydraulic system resistance, that can be determined analyzing experimental data and equipment uncertainty. Other sources of uncertainties, that affect the flow field in a pump, are the uncertainties on the turbulence quantities. The turbulence intensity and the viscosity ratio are the parameters that characterizes a turbulent flow, but them values are not uniquely determinable. In this study the turbulence parameters vary in a range according to the best practice for a centrifugal pump. In Table 8 the range of uncertainty for the four uncertain variables are summarized. An uniform Probability Density Function (PDF) is defined for each uncertainty. The optimum found by the SBO with SOGA is considered as the deterministic optimum.

To comply with the formulation within the CFD solver, the boundary conditions must be expressed in terms of rotational speed and flow rate. Given the pump and system curves for a fixed rotational speed and hydraulic resistance, respectively, the flow rate is derived by intersecting the two curves. The pump curves for the baseline and the optimum are computed using CFD (see Fig. 13), while the system curve is estimated as $\Delta p_{Tot} = a \cdot Q^2$, *i.e.* a parabola passing through the working point, where the parameter a is proportional to the system resistance. This formulation allows to apply uncertainty to the system resistance varying the parameter a. Using Fig. 13, the minimum and the maximum value of the flow rate given by the uncertainties of the rotational speed and the system resistance are obtained. To simplify the problem, a uniform PDF for the flow rate is considered, even if this is equivalent to consider a wider uncertainty on the resistance (see Fig. 14). This simplification is accepted because i) it ensures higher safety, and ii) the error of the uncertainty is small.

To assess the robustness of the optimal design and of the baseline, a Polynomial

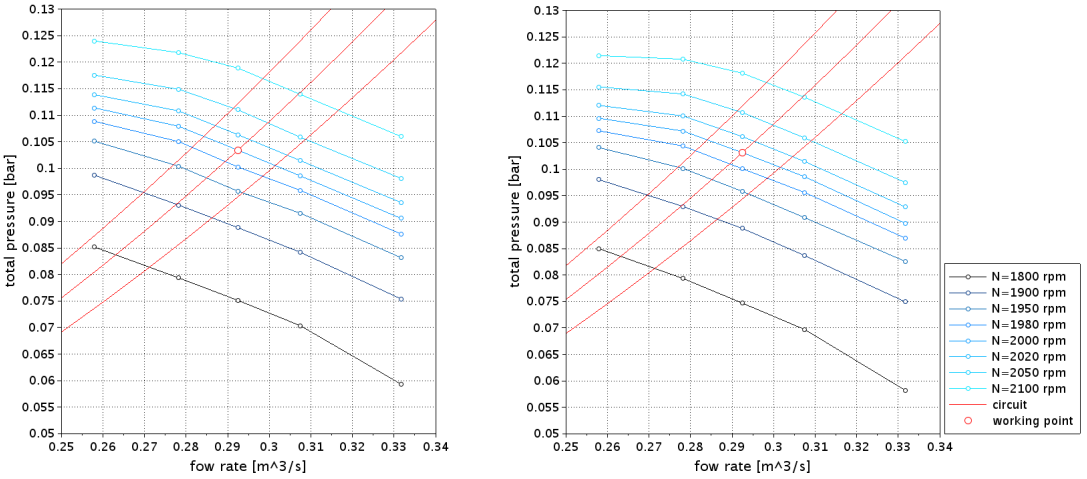

(a) *Total pressure head curves of the baseline and system curves*

(b) *Total pressure head curves of the optimum and system curves*

Figure 13.: Pump curves of the baseline (left) and the optimum (right) and system curves

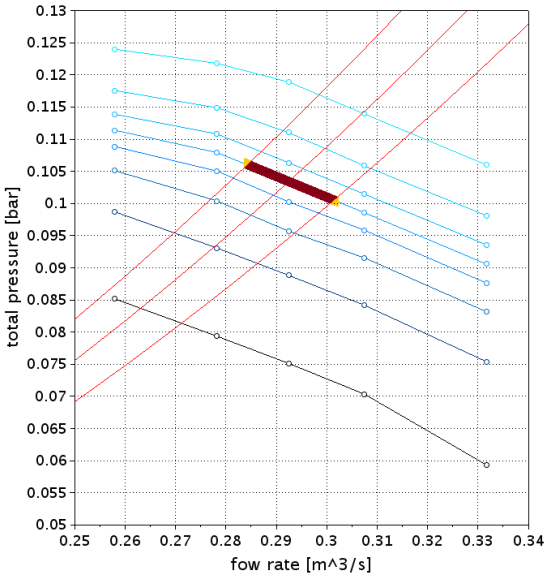

Figure 14.: Area of uncertainty: in dark red uncertainty given by the rotational speed and the system resistance, in yellow the uncertainty added considering the flow rate instead of the system resistance

Geometry	μ_ψ [-]	σ_ψ [-]	μ_η [%]	σ_η [%]
baseline	0.889	0.016	91.3	0.25
optimum	0.888	0.015	94.8	0.24

Table 9.: Mean and standard deviation of the performances PDF of the baseline and the optimum

Chaos Expansion (PCE) [21], which is a well-known technique for propagating uncertainties at low computational cost, is employed. It is based on a multidimensional orthogonal polynomial approximation in terms of standardized random variables. A one-to-one correspondence exists between the choice of stochastic variable and the polynomials. For instance, if a normal/uniform variable is considered, the corresponding polynomials are Hermite/Legendre polynomials. The random output R is given by a finite-dimensional series expansion:

$$R = \sum_{i=0}^{P} \alpha_i \Psi_i(\xi), \tag{1}$$

where Ψ_i are the multidimensional orthogonal polynomials. They are derived from the family of hyper-geometric orthogonal polynomials or Askey scheme [22]. The α_i are deterministic coefficients of the expansion, computed through a multidimensional integration. A tensor product of Gaussian quadrature rule of forth order is employed to obtain the expansion coefficients, for a total of 625 evaluations.

Statistics as mean and standard deviation can be computed analytically from the expansion. To evaluate the PDF of the output a Monte Carlo sampling can be performed directly on the polynomial approximation, which is a surrogate model of the function of interest with respect to the input parameters.

7. Uncertainty Quantification assessment results

A PCE is computed for the baseline and the optimum to assess the robustness of the performances. The mean μ and the standard deviation σ of the total pressure coefficient and the efficiency are calculated analytically and they are shown in Tab. 9. Notice that mean values are basically equal to the performances of the related design: the main discrepancy is on the mean efficiency that is 0.2% and 0.1% lower than the expected value respectively for the baseline and the optimum. Moreover, the standard deviation of the efficiency is for both the design sufficiently small to confirm the deterministic improvement of the optimum, even under uncertain operating conditions. The standard deviation of the total pressure coefficient is equal to the 1.8% of the mean and can not be ignored when constraining the working point.

The PDF, which are estimated through a Monte Carlo sampling on the polynomial expansion and a Kernel Density Estimation (KDE), are also considered (see Fig. 15). The remarks based on the previous statistics are confirmed: i) the efficiency of the optimal design is always higher than the baseline efficiency, and ii) the two design have the same pressure head PDF. The change in total pressure coefficient, even if not negligible, does not break the constraint. In addition, the shape of the PDF for the optimum and the baseline are compared in Fig. 16. Here the PDF are plotted so that the mean values are shifted in zero. The baseline efficiency shows a little

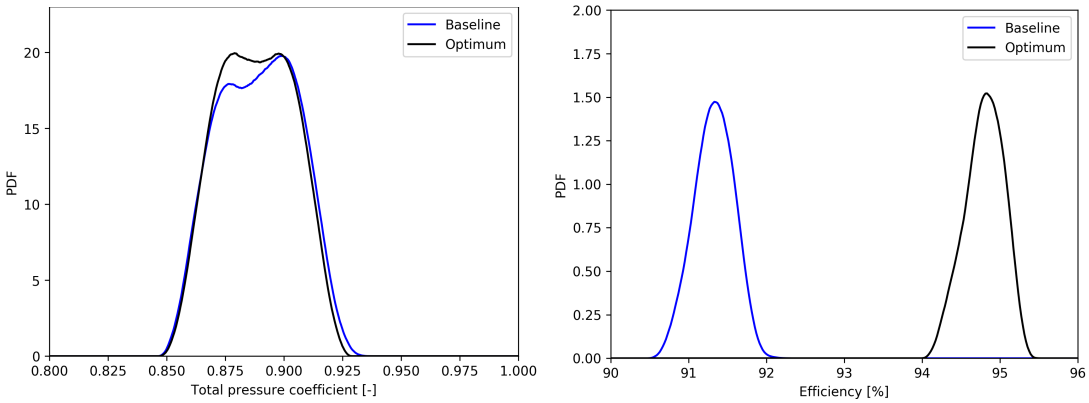

Figure 15.: Comparison of the PDF of the total pressure coefficient (left) and the efficiency (right), related to the baseline and the optimum

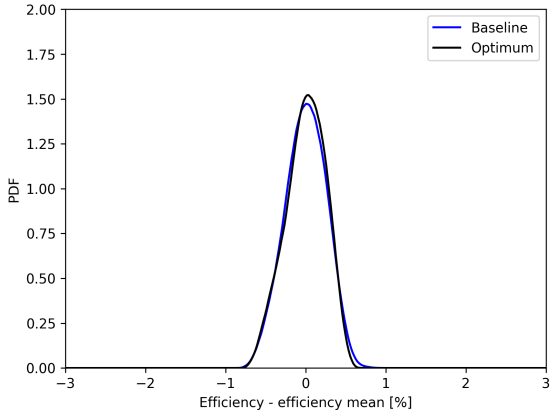

Figure 16.: Comparison of the PDF shape of the baseline and the optimum

more pronounced tail on the right side of the distribution, but the two PDF are in substance similar, suggesting that the robustness of the design performances are not effected significantly by the optimization.

Computing a PCE assesses to have for free the evaluation of the Sobol indices for the four uncertain variables respect to the total pressure coefficient and the efficiency. The results are shown in 10. The variability of the total pressure coefficient is mainly affected by only the system resistance.

8. Conclusions

A framework to assess the robustness of the optimum under uncertainty is presented.

First a deterministic optimization is carried out through two different surrogate-based optimization strategies: SBO with SOGA and EGO. The SBO with SOGA reaches an optimal design with an efficiency $\eta = 94.9\%$, corresponding to an improvement about 3.4% with respects to the baseline. The EGO scouts a wider area of the input space, but it doesn't improve the SOGA result, returning an optimum with an efficiency $\eta = 94.6\%$. The two efficiencies are comparable even though the two design show some differences. This confirms the reability of the SOGA optimum, that is considered in the further study.

Starting from this result, a robustness analysis of the design under uncertainty is

Uncertain variable	ψ total Sobol' index		η total Sobol' index	
	Baseline	Optimum	Baseline	Optimum
Rotational speed N	$5.86e-02$	$6.06e-02$	$3.69e-01$	$3.73e-01$
System resistance a	$9.37e-01$	$9.38e-01$	$4.68e-01$	$5.57e-01$
Turbulent intensity I	$4.51e-03$	$1.43e-03$	$1.26e-01$	$4.19e-02$
Viscosity ratio $\frac{\mu_T}{\mu}$	$1.09e-03$	$1.67e-03$	$8.67e-02$	$5.13e-02$

Table 10.: Total Sobol' index

performed. In fact, uncertainty occurs in every field. In this work, the focus is on the epistemic uncertainty related to the experimental tests, used to verify the performances of the pump. In particular, the main sources of uncertainty of the test rig are the rotational speed of the pump and the hydraulic resistance of the system.

A polynomial chaos expansion is employed to assess the influence of the operation conditions uncertainties on the efficiency and the total pressure coefficient. The two objective functions PDF of the baseline and the optimum are compared. From this analysis the optimum is robust in terms of efficiency and comparable to the baseline in terms of total pressure head. This validate the result of the deterministic optimization even if uncertainties on the operation conditions are present.

9. Acknowledgement

Research carried out with the support of resources of Big&Open Data Innovation Laboratory (BODaI-Lab), University of Brescia, granted by Fondazione Cariplo and Regione Lombardia

References

[1] Van Den Braembussche, R. A. (2006) Optimization of radial impeller geometry. In: Design and Analysis of High Speed Pumps, number RTO-EN-AVT-143. RTO of NATO.

[2] Pasquale, D., Ghidoni, A., and Rebay, S. (2013) Shape optimization of an organic rankine cycle radial turbine nozzle. Journal of Engineering for Gas Turbines and Power 135(4), 042308-042308-13.

[3] Guo, Z., Song, L., Zhou, Z., Li, J., and Feng, Z. (2015) Multi-objective aerodynamic optimization design and data mining of a high pressure ratio centrifugal impeller. Journal of Engineering for Gas Turbines and Power 137(9), 092602-092602-14 09.

[4] Verstraete, T., Alsalihi, Z., and Van den Braembussche, R. A. (2010) Multidisciplinary optimization of a radial compressor for microgas turbine applications. Journal of Turbomachinery 132(3), 031004-031004-7 03.

[5] Olivero, M., Pasquale, D., Ghidoni, A., and Rebay, S. (2014) Three-dimensional turbulent optimization of vaned diffusers for centrifugal compressors based on metamodel-assisted genetic algorithms. Optimization and Engineering 15(4), 973-992.

[6] Pei, J., Wang, W., and Yuan, S. (2016) Multi-point optimization on meridional shape of a centrifugal pump impeller for performance improvement. Journal of

Mechanical Science and Technology 30(11), 4949-4960 Nov.

[7] Wang, W., Pei, J., Yuan, S., Zhang, J., Yuan, J., and Xu, C. (2016) Application of different surrogate models on the optimization of centrifugal pump. Journal of Mechanical Science and Technology 30, 567-574 02.

[8] De Donno, R., Ghidoni, A., Noventa, G., and Rebay, S. (2019) Shape optimization of the ercoftac centrifugal pump impeller using open-source software. Optimization and Engineering.

[9] Beyer, H.-G. and Sendhoff, B. (2007) Robust optimization a comprehensive survey. Computer Methods in Applied Mechanics and Engineering 196(33), 3190-3218.

[10] Stepanoff, A. (1993) Centrifugal and axial flow pumps. Krieger Publishing Company.

[11] Ghidoni, A., Pelizzari, E., Rebay, S., and Selmin, V. (2006) 3d anisotropic unstructured grid generation. International Journal for Numerical Methods in Fluids 51(9-10), 1097-1115.

[12] foam-extend, 4.1 edition. `https://sourceforge.net/projects/foam-extend/`.

[13] Menter, F. (1993) Zonal Two Equation k-w Turbulence Models For Aerodynamic Flows. Fluid Dynamics and Co-located Conferences. American Institute of Aeronautics and Astronautics AIAA Jul.

[14] Petit, O., PAGE, M., Beaudoin, M., and Nilsson, H. (2009) The ercoftac centrifugal pump openfoam case-study. 01.

[15] De Donno, R., Rebay, S., and Ghidoni, A. (2019) Surrogate-based shape optimization of the ercoftac centrifugal pump impeller. Computational Methods in Applied Sciences 49, 227-246.

[16] Eldred, M. and Dunlavy, D. Formulations for surrogate-based optimization with data fit, multifidelity, and reduced-order models. In: 11th AIAA/ISSMO Multidisciplinary Analysis and Optimization Conference.

[17] Giunta, A., Swiler, L., Brown, S., Eldred, M., Richards, M., and Cyr, E. The surfpack software library for surrogate modeling of sparse irregularly spaced multidimensional data. In: 11th AIAA/ISSMO Multidisciplinary Analysis and Optimization Conference (AIAA Paper 2006-7049, Portsmouth, VA, 2006).

[18] Li, Z. and Zheng, X. (2017) Review of design optimization methods for turbomachinery aerodynamics. Progress in Aerospace Sciences 93, 1-23.

[19] Jones, D. R., Schonlau, M., and Welch, W. J. (1998) Efficient global optimization of expensive black-box functions. Journal of Global Optimization 13(4), 455-492 Dec.

[20] Dakota, 6.8 edition. `https://dakota.sandia.gov/`.

[21] Wiener, N. (1938) The homogeneous chaos. American Journal of Mathematics 60(4), 897-936.

[22] Askey, R. and Wilson, J. (1985) Some basic hypergeometric orthogonal polynomials that generalize Jacobi polynomials. Memoirs of the American Mathematical Society. American Mathematical Society, Providence, RI.